

# Role of the Electron–Dipole Interaction in Photodetachment Angular Distributions

C. Annie Hart, Justin Lyle, Joseph Spellberg, Anna I. Krylov, and Richard Mabbs\*



Cite This: *J. Phys. Chem. Lett.* 2021, 12, 10086–10092



Read Online

ACCESS |



Metrics & More

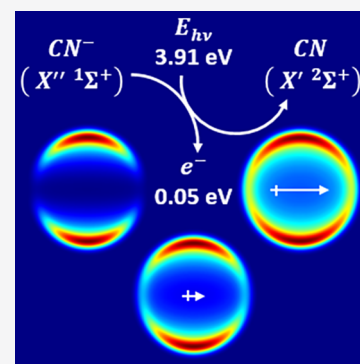


Article Recommendations



Supporting Information

**ABSTRACT:** The importance of including long-range electron–molecule interactions in treatments of photodetachment and/or photoionization is demonstrated. A combined experimental and computational study of  $\text{CN}^-$  detachment is presented in which near threshold anisotropy parameters ( $\beta$ ) are measured via photoelectron imaging. Calculated  $\beta$  values, based on an EOM-IP-CCSD/aug-cc-pVTZ Dyson orbital, are obtained using free-particle and point dipole models. The results demonstrate the influence of the molecular dipole moment in the detachment process and provide an explanation of the recently reported near threshold behavior of the overall photodetachment cross section in  $\text{CN}^-$  detachment.



Photoelectron angular distributions (PADs) represent sensitive probes of bound electronic structure and metastable excited states (electronic resonances) for systems with a single negative charge. The anisotropy parameter,  $\beta$ , describes the PAD in relation to the electric vector of a linearly polarized photon in a single photon detachment.  $\beta$  encodes all of the details of the detachment process, but disentangling the contributing factors is not trivial. A distinction is usually made between direct detachment (sudden electron ejection to the continuum) and indirect detachment (electron loss via autodetaching excited anion states). The final states of the electron ejected via these processes are different, giving rise to different PADs. Differences between the expected  $\beta$  for photoelectrons ejected via direct detachment and experimental measurement are then used to infer the existence of a resonance. Unfortunately, calculations of  $\beta$  are challenging, and the results obtained with simple models are often in quantitative disagreement with experiment. In this contribution, we use  $\text{CN}^-$  detachment to highlight this problem and to show how computational treatment can be improved.

Within the dipole approximation, cross sections for direct detachment, which describe the probability of photoelectron ejection in a certain direction, are expressed in terms of photoelectron matrix elements

$$D_k = \mathbf{u} \langle \Psi_F^{N-1} \psi_k^{\text{el}} | \mu | \Psi_I^N \rangle \quad (1)$$

where  $\mu$  is the dipole moment operator,  $\mathbf{u}$  is a unit vector along the polarization of light,  $\Psi_I^N$  and  $\Psi_F^{N-1}$  denote the initial (anionic) and final (neutral) states, respectively, and  $\psi_k^{\text{el}}$  is the wave function of the ejected electron with momentum  $k$ . Both  $\Psi_I^N$  and  $\Psi_F^{N-1}$  are many-body wave functions, but their explicit

knowledge is not required for computing matrix elements of the dipole moment operator; the expression for the photoelectron dipole moment can be written in the following (equivalent, under the assumption of strong orthogonality) form:

$$D_k = -\mathbf{u} \langle \phi^{\text{d}}(\mathbf{r}) | \mathbf{r} | \psi_k^{\text{el}}(\mathbf{r}) \rangle \quad (2)$$

where  $\phi^{\text{d}}(\mathbf{r})$  is a one-electron function, called a Dyson orbital, which contains all of the necessary information about molecular states before and after photodetachment:

$$\phi^{\text{d}}(1) = \sqrt{N} \int \Psi_F^{N-1*}(2, \dots, N) \Psi_I^N(1, \dots, N) d2 \dots dN \quad (3)$$

This rigorous quantum-mechanical result, which stems from the indistinguishability of the electrons, allows one to interpret electron ejection from a correlated many-body system within a one-electron framework. The concept of the Dyson orbital (or generalized overlap) goes beyond Koopmans' approximation, while retaining the insight associated with a one-electron-like treatment. In particular, eq 2 gives rise to dipole selection rules for photodetachment (and photoionization), as illustrated for atomic detachment in Figure 1.

In atomic detachment, the angular momentum of the Dyson orbital defines the angular momentum of the outgoing electron.

Received: September 1, 2021

Accepted: October 4, 2021

Published: October 8, 2021



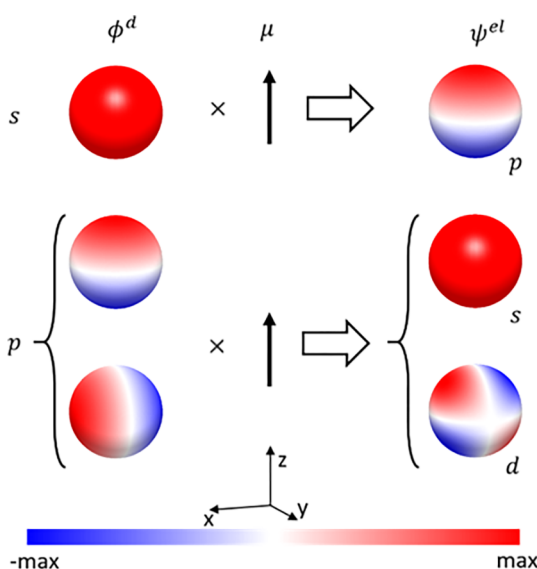


**Figure 1.** Dipole selection rules in photoionization/photodetachment. Angular components of the Dyson orbital are shown in the left-hand column, and angular components of the photoelectron wave function are shown in the right-hand column (amplitudes illustrated on the surface of a sphere). In accordance with angular momentum conservation ( $\Delta l = \pm 1$ ), ionization/detachment from an s orbital (first row) yields a pure p wave. Detachment from a p orbital (second and third rows) yields interfering s and d waves.

The relative weights of different partial waves can be understood by the Wigner threshold law.<sup>1,2</sup> In the case of molecular photodetachment, Dyson orbitals have complicated shapes, yet general trends in PADs can be predicted by representing molecular Dyson orbitals as a linear combination of atom-like orbitals.<sup>3–6</sup>

Quantitative treatments for  $\beta$  must include two essential parts: (1) accurate representation of the parent electronic structure, including accurate and balanced treatment of electron correlation in the initial and final states as well as orbital relaxation resulting from the removal of the excess electron, and (2) an accurate description of the photoelectron state. The first requirement can be satisfied by using high-level treatments of many-body wave functions, such as, for example, equation-of-motion coupled-cluster methods, to compute the Dyson orbital associated with the detachment transition.<sup>7–9</sup> The second requirement, accurate treatment of the free-electron state, is more difficult to achieve. The simplest approximation assumes that the photoelectron does not experience the effect of the remaining neutral core and, therefore, can be approximated by a plane wave (free-particle solutions to the Schrödinger equation). This neglect of the interactions between the continuum electron and molecular core is often justified by the photoelectron state's large size relative to the molecule. Using this treatment of photoelectrons, one can easily compute photoelectron matrix elements (and, consequently, differential and overall cross sections for photodetachment) for a given Dyson orbital.<sup>10–12</sup> This approach is implemented in the ezSpectra suite of programs,<sup>12</sup> in which the ezDyson<sup>10</sup> module provides a convenient means to calculate  $\beta$  values from *ab initio* Dyson orbitals.

More rigorous treatments of the free-electron state entail solving the one-electron Schrödinger equation with an effective Fock-like potential representing the molecular core. While such advanced treatments can capture the effect of the perturbation of

the core on the free electron (for example, ref 9), the calculations are far from routine and the respective codes are not black-box. Here we show that the simplest plane-wave model can be significantly improved by including the effect of a point dipole. These results provide a simple physical illustration of the effect and suggest a possible route to building hierarchical improvements for the plane-wave model of photodetachment.

This work presents the experimentally measured variation in  $\beta$  as a function of excitation energy in the near threshold region for the  $\text{CN}^-(X''^1\Sigma^+) \rightarrow \text{CN}(X'^2\Sigma^+) + e^-$  transition.  $\text{CN}^-$  is chosen for a number of reasons. The threshold energy is well-known;<sup>13</sup> neutral CN has a relatively high dipole moment,<sup>14</sup> and there are no accessible, near threshold resonances.<sup>15,16</sup> We show that free-electron model predictions significantly deviate from the experimental results at low photoelectron energies. On the contrary, including a point dipole in the treatment of the continuum clearly demonstrates the importance of interaction between the residual polar neutral CN and the photoelectron. We further show that the model also offers an explanation for the recently reported temperature-dependent changes in the overall detachment cross section for  $\text{CN}^-$ .<sup>17</sup>

Photoelectron images for  $\text{CN}^-$  detachment were collected using photon energies ranging from 3.87 to 4.40 eV (experimental and data processing/analysis details can be found in Supporting Information S11). Each image contains a single electronic band, from the anion ground state to the neutral ground state ( $X''^1\Sigma^+ \rightarrow X'^2\Sigma^+$ ). There is no obvious vibrational structure visible within this band, consistent with the similarity between the neutral and anion ground state equilibrium bond lengths and the large vibrational frequencies.<sup>13</sup> At photon energies significantly above threshold, the photoelectron intensity shows a distinct preference for polarization along the electric vector of the radiation. In broad terms, this is the expectation for detachment from a  $\sigma$ -molecular orbital. However, the degree of polarization within the PAD shows marked variation as a function of photon energy.

The PAD for linearly polarized, sudden, one-photon detachment is represented as  $I(\theta) \propto 1 + \beta P_2(\cos \theta)$ .  $P_2(\cos \theta)$  is the second Legendre polynomial, and  $\beta$  is the anisotropy parameter that quantitatively describes the distribution. Figure 2 shows mean  $\beta$  values recorded at different photon energies ( $h\nu$ ) for  $\text{CN}^-$  detachment. The data are displayed as a function of electron kinetic energy (eKE), which increases linearly with  $h\nu$  according to the equation  $\text{eKE} = h\nu - \text{EA}$ . Because the images show a single detachment transition, the electron affinity (EA) of CN (3.862 eV)<sup>13</sup> is used to determine the eKE and calibrate the detector. Each point in Figure 2a incorporates at least 12, and on average 34, individual  $\beta$  values, where each quadrant of an image represents a measurement. The error bars reflect one standard deviation from the mean within these measurements, giving an idea of the repeatability of the data. Positive  $\beta$  values indicate polarization of the photoelectron distribution along  $\epsilon_p$ , with the limiting  $\beta = +2$  representing a parallel distribution. As shown in Figure 2a,  $\beta$  shows a relatively rapid rise from near zero (isotropic) at a very low eKE to around 1.8 at an eKE of >0.4 eV. There is a possible hint of a minimum around 0.35 eV. Reasons for this are unclear, and given the error bars in this region, ascribing significance to this risks overinterpretation of the available data.

The data of Figure 2 are associated with the  $\text{CN}^-(X''^1\Sigma^+) \rightarrow \text{CN}(X'^2\Sigma^+) + e^-$  transition. The associated Dyson orbital (shown in Figure 3) is computed using EOM-IP-CCSD<sup>18</sup> wave functions of the neutral and CCSD wave function of the anion,

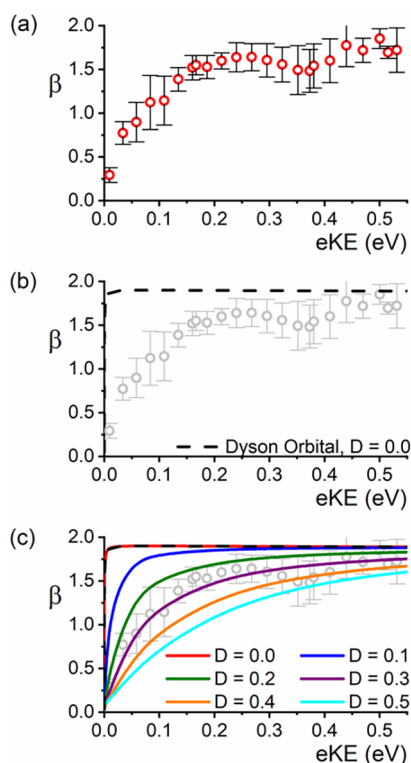


**Figure 2.** (a) Mean  $\beta$  vs eKE for the  $\text{CN}^-(X^1\Sigma^+) \rightarrow \text{CN}(X^2\Sigma^+) + e^-$  transition. Each point represents an average over at least 12 measurements, and the error bars are one standard deviation from the mean. (b) The dashed line shows the computed  $\beta$  as a function of eKE using the Dyson orbital associated with the transition and in the free-electron (zero dipole moment) limit. (c) The solid curves show the computed  $\beta$  as a function of eKE for detachment from the  $\text{CN}^-$  (yielding the  $X^2\Sigma^+$  state of the neutral) as the dipole moment ( $D$ ) is increased from 0 to 0.5 a.u.

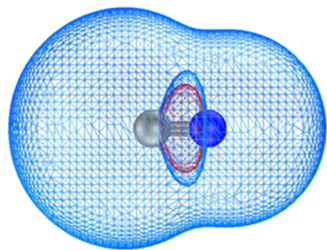


**Figure 3.** Dyson orbital (isovalue of 0.02) for the  $\text{CN}^-(X^1\Sigma^+) \rightarrow \text{CN}(X^2\Sigma^+) + e^-$  transition.

with the aug-cc-pVTZ basis set. The calculations were carried out using the Q-Chem package.<sup>19</sup> The orbital is of  $\sigma$  character, and its shape can be described as s-like, suggesting production of a photoelectron of predominantly  $p_z$  character. Such an outgoing photoelectron wave function would produce an angular distribution with a highly positive  $\beta$ . However, the cylindrical symmetry introduces some p character into the Dyson orbital and, hence, a non-negligible s wave component in the outgoing wave function. This effect should be most obvious in the near threshold limit due to the centrifugal barrier to detachment. The observation of a near isotropic distribution ( $\beta \approx 0$ ) close to threshold, which becomes more polarized as the electron kinetic energy increases, is qualitatively consistent with detachment from the  $\sigma$ -type orbital.

Although the qualitative agreement is good, the finer physics of the detachment process are revealed only through a quantitative treatment.  $\beta$  can range from  $>0$  to 2 for distributions polarized parallel to  $\epsilon_p$ . The extent of the polarization depends on a number of factors, including, but not limited to, the nature of the parent orbital. Other factors that influence the final distribution are the presence of excited but unstable anion states and long-range interactions between the neutral residue and outgoing electron.

The dashed black line of Figure 2b represents  $\beta$  values calculated using the EOM-IP-CCSD/aug-cc-pVTZ Dyson orbital of Figure 3. The  $\beta$  values are determined using ezDyson,<sup>10,12</sup> treating the electron as a free particle. The calculations are in excellent agreement with the qualitative expectations outlined above ( $\beta$  rises very rapidly from zero at threshold). However, the quantitative agreement with experiment in the near threshold region is poor.

Deviations between expected and measured PADs often indicate a mediating resonance (metastable anion state). However, there is sufficient theoretical evidence that this is not the case for  $\text{CN}^-$  detachment. Both CAP-EOM-CCSD<sup>16</sup> and R-Matrix scattering calculations<sup>15</sup> show the lowest excited anion states of  $\text{CN}$  are too high in energy to affect the near threshold PADs.

The quantitative treatment of  $\beta$  rests on calculating the photoelectron matrix element,  $D_k(\theta_k\phi_k)$ , where the laboratory frame PADs,  $I(\theta) \propto |D_k(\theta_k\phi_k)|^2 \propto 1 + \beta P_2(\cos \theta_k)$ . For photodetachment via a linearly polarized photon,  $D_k(\theta_k\phi_k)$  is required for only two directions,  $\theta_k = 0$  and  $\pi/2$ , for a given linear momentum  $k$ . In practice, the problem boils down to evaluating the molecular frame integrals,  $\langle \psi_k^{\text{el}} | r Y_{1,m} | \phi^{\text{d}} \rangle$ , where  $Y_{1,m}$  is the projection of the photon angular momentum onto the molecule frame axes,  $\phi^{\text{d}}$  is the Dyson orbital for the detachment transition, and  $\psi_k^{\text{el}}$  is the photoelectron wave function. These molecular frame integrals are evaluated over the spatial coordinates of the electron. Subsequent transformation to the lab frame and averaging over molecular orientations allow the determination of  $\beta$  for isotropically averaged molecular orientations.<sup>10,11,20</sup>

In the following, we assume that the EOM-IP-CCSD/aug-cc-pVTZ treatment of the parent orbital is accurate so that the main discrepancies between prediction and experiment must arise from the treatment of the continuum wave function.

In the free-electron approximation, the photoelectron wave function is given by the plane wave, which can be represented in terms of the partial waves (pure angular momentum solutions of the free-particle solutions of the Schrodinger equation). Expanding the plane wave in terms of spherical harmonics<sup>21</sup>

$$\psi_k^{\text{el}} = 4\pi \sum_l \sum_\lambda j_l(kr) Y_{l,\lambda}(\hat{\mathbf{r}}) Y_{l,\lambda}^*(\hat{\mathbf{k}}) e^{i\mathbf{k}\cdot\mathbf{r}} \quad (4)$$

allows decomposition into the individual, pure orbital angular momentum components (partial waves) of the photoelectron wave function. This also allows simplification of the photoelectron matrix element calculations (via the angular momentum selection rules).

The free-electron approximation ignores any interaction between the departing electron and the neutral residue. This is justified when the longer-range contributions to the effective potential decrease faster than  $1/r^2$ , or for high-angular momentum components to the photoelectron wave function. However, the electron-dipole interaction varies with  $1/r^2$  and has a significant bearing on the continuum wave functions, and

hence PADs associated with detachment producing polar molecules.

Approximating the molecular dipole as a point dipole allows a simple demonstration of the effect on the continuum. The photoelectron wave function can be expanded in terms of the solutions of the point dipole Schrodinger equation (which are known, although not necessarily that familiar to experimental chemists! Details can be found in [Supporting Information S12](#)).<sup>22,23</sup> This shows that the dipole moment mixes orbital angular momentum components to the effect that orbital angular momentum is no longer a conserved quantity ( $l$  is no longer a good quantum number). For the point dipole,  $\lambda$ , representing the component of the orbital angular momentum on the dipole axis is still a good quantum number. To represent the orbital angular momentum, in place of the integer  $l$  quantum number, the non-integer  $L_N^\lambda$  is used, where  $N$  is an integer index. Each  $L_N^\lambda$  therefore correlates to a pure  $l, \lambda$  combination in the zero dipole limit. The effect of the dipole moment on the continuum state is illustrated in [Figure 4](#) for  $\lambda = 0$ .

The contour lines of [Figure 4](#) represent the amplitude of the  $L_0^0$  and  $L_1^0$  wave functions, with the point dipole located at the origin (indicated by the white dot), with the positive end to the left. The illustrations are for an eKE of 0.1 eV and three selected dipole moments (indicated to the extreme left in atomic units).

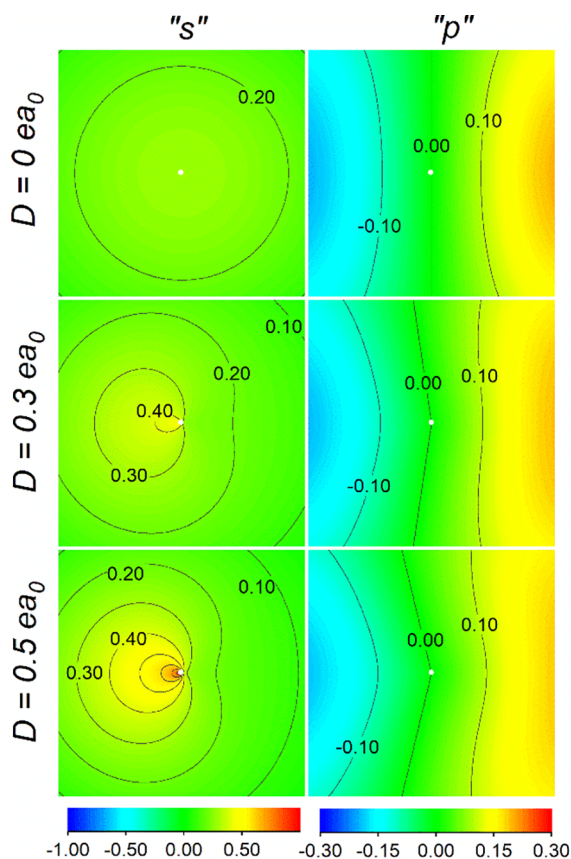


**Figure 4.** Effect of an increasing dipole moment on the photoelectron state. Contours represent the amplitudes of the point dipole functions. The left column represents the effect of a point dipole (located at the white dot in the center of each plot) on the continuum function correlating with a free-electron s-wave. The right column shows the effect of a point dipole on the continuum function correlating to a  $p_0$  electron wave. The (selected) dipole moments are shown at the left in atomic units.

The first column represents the effect on the continuum function correlating with the free-particle (zero-dipole moment) limit s-wave ( $l = 0, \lambda = 0$ ), while the second column represents the function correlating with to a  $p_0$  wave ( $l = 1, \lambda = 0$ ). The first row of [Figure 4](#) illustrates the free-particle amplitudes. Increasing the dipole moment mixes different  $l$  components, distorting the pure angular momentum wave, an effect that clearly increases with the magnitude of the dipole moment. The effect is greatest for lower, zero-dipole limit  $l$  values (i.e., the s- and p-waves) due to the centrifugal contribution to the effective potential. Higher  $l$  waves are suppressed near the point dipole origin.

To quantify the effect of the point dipole on the PAD, we can proceed as follows (more details can be found in [Supporting Information S13](#)). By direct analogy to the free-electron case ([eq 4](#)), the photoelectron wave function is expanded in terms of the solutions of the point dipole Schrodinger equation

$$\psi_k^{\text{el}} = 4\pi \sum_N \sum_\lambda f_{N\lambda}(kr) \Omega_{L_N^\lambda}(\hat{\mathbf{r}}) \Omega_{L_N^\lambda}^*(\hat{\mathbf{k}}) e^{iL_N^\lambda \pi/2} \quad (5)$$

The point dipole angular functions,  $\Omega_{L_N^\lambda}$  can be further expanded in terms of spherical harmonics

$$\Omega_{L_N^\lambda} = \sum_{l=0}^{\infty} A_{L_N^\lambda, l} Y_{l, \lambda} \quad (6)$$

The expansion coefficients,  $A_{L_N^\lambda, l}$ , are the eigenvector coefficients of the tridiagonal matrix

$$\langle Y_{l', \lambda}(\theta_l, \phi_l) | l'^2 - 2D \cos \theta_l | Y_{l, \lambda}(\theta_l, \phi_l) \rangle \quad (7)$$

where  $D$  represents the strength of the dipole moment and  $\theta_l$  is the angle between the dipole axis and the electron's position vector. The eigenvalues are  $L_N^\lambda(L_N^\lambda + 1)$ , where  $L_N^\lambda$  is non-integer when  $D > 0$ .

The radial functions in [eq 5](#) are

$$f_{N\lambda}(kr) = \alpha_{N\lambda} r \sqrt{k} j_{L_N^\lambda}(kr) \quad (8)$$

where  $\alpha_{N\lambda}$  is a normalization constant,  $k$  is the electron momentum, and  $j_{L_N^\lambda}(kr)$  is a spherical Bessel function.

[Figure 2c](#) shows the results of substitution for the point dipole expansion of the photoelectron wave function in the calculation of the photoelectron matrix element. The calculations are performed using the Dyson orbital of [Figure 3](#), as in the case of plane-wave treatment (by ezDyson) described above. The results are shown as solid lines in [Figure 2c](#), which represent the variation in  $\beta$  with eKE for different dipole moment values  $D$  (in atomic units), between 0 and 0.5 a.u.

The  $D = 0$  results (solid red line) are identical to the ezDyson calculation of [Figure 2b](#) (dashed black line). This is to be expected; the point dipole expansion is exactly equivalent to the plane-wave expansion in the limit of zero dipole moment. However, as  $D$  increases, the effect on the angular distributions is clear. In the near threshold region,  $\beta$  rises less steeply as the dipole moment increases, following the essential trends in the observed behavior.

Using the point dipole approximation, we have illustrated how the electron–dipole interaction affects photodetachment. The angular and radial components of the photoelectron wave functions are separable, and  $\lambda$  is a good quantum number, allowing relatively simple evaluation of the photoelectron matrix elements. Although the model and experimental data are in

excellent agreement for  $D = 0.3$  a.u., this should be viewed with caution. The actual dipole moment of CN is  $1.45 D$ ,<sup>14</sup>  $0.57$  a.u., and the point dipole model effectively overestimates the effect of the neutral residue's dipole moment.

From the perspective of the photoelectron, a point dipole should be a reasonable representation at large distances. However, calculation of the photoelectron matrix element integrals (especially for low-eKE and lower-angular momentum components) involves integrands with significant contributions near the origin, precisely where the point dipole approximation is least appropriate. Similarly, the continuum functions used depend only on the dipole moment of the neutral CN molecule at equilibrium. This neglects perturbation of the neutral charge density distribution by the outgoing electron and effectively assumes the remaining bound electrons rearrange more rapidly than the photoelectron is ejected. The extent of these effects on the calculated  $\beta$  requires further investigation.

Another complicating factor is the use of a fixed dipole. The fixed dipole limit for a dipole bound state is  $1.625 D$  ( $0.639$  a.u.),<sup>24,25</sup> but molecular rotation has long been known to increase the dipole moment actually required to bind an electron.<sup>26–28</sup> It is not easy to incorporate the effect of molecular rotation. On one hand, the electronic excitation is rapid compared to the time scale of rotation and the photoelectron matrix elements are determined using the continuum associated with the neutral CN molecule at a particular orientation. On the other hand, as the electron departs the continuum functions may well be affected by rotation of the molecular dipole. The net result is presumably to effectively lower the dipole moment used in the determination of the photoelectron matrix element.

The influence of molecular rotation can be tested through measurements at different temperatures. Accurate control of the ion temperature is currently beyond the capability of our instrumentation. However, near threshold measurements of the overall detachment cross section ( $\sigma$ ) for  $\text{CN}^-$  have recently been reported at two temperatures, 16 and 295 K.<sup>17</sup> The overall cross sections at a given photon energy are the sum of the cross sections for all rovibronic channels ( $\sigma_{hv}^{J'' \rightarrow J'k}$ ), which are related to the photoelectron matrix elements as (Supporting Information S14)

$$\sigma_{hv}^{J'' \rightarrow J'k} \propto P(J'', T) |C_{000}^{J'' J'}|^2 \int_0^{2\pi} d\theta_k \int_0^\pi d\theta_k \sin \theta_k |D_k(\theta_k \phi_k)|^2 \quad (9)$$

where  $P(J'', T)$  is the population of the  $J''$  rotational level of the anion at temperature  $T$ ,  $C_{000}^{J'' J'}$  is a Clebsch–Gordan coefficient, and  $k$  is different for each open channel. The integrals over  $\theta_k$  and  $\phi_k$  are performed in the molecule frame. In ref 17, the experimental data are fit to the expression

$$\sigma \propto \sum_{J''} \sum_{J'} P(J'', T) |C_{000}^{J'' J'}|^2 (e\text{KE})^n \quad (10)$$

The integrals of eq 9 for each channel are replaced with an  $n^{\text{th}}$  power dependence of the channel's electron kinetic energy. Comparison with experiment is achieved in ref 17 using a scaling factor, which represents (along with  $n$ ) a free parameter in fitting eq 10 to the experimental data.

The experimental cross section trends are reproduced in the gray solid curves of Figure 5, using the reported  $n$  of 0.46 at 16 K (Figure 5a). In Figure 5b, the 295 K results are represented using an  $n$  of 0.7, a compromise between the values reported from two different sets of apparatus.<sup>17</sup> Panels c and d of Figure 5 (16 and

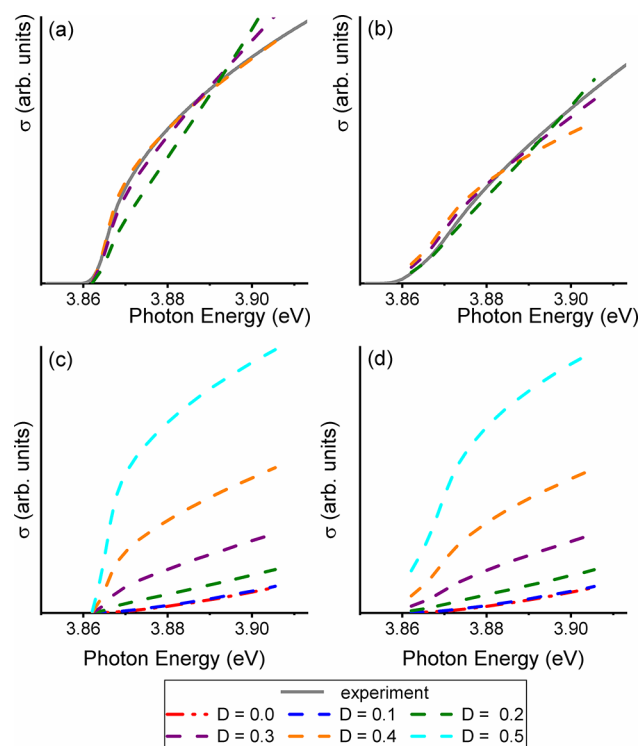


**Figure 5.** Experimental<sup>17</sup> (gray solid lines) and point dipole results (dashed lines) of the overall detachment cross section  $\sigma$  as a function of photon energy: (a and c) 16 K and (b and d) 295 K. The dipole moments ( $D$ ) are given in atomic units.

295 K, respectively) show the overall cross section results of the point dipole model. The dashed curves represent the variation in  $\sigma$  with photon energy for dipole moments, from  $D = 0.0$  to  $D = 0.5$  a.u. in increments of 0.1 a.u. The dipole moment clearly alters the near threshold behavior. As the dipole moment increases,  $\sigma$  increases more rapidly. Comparisons with the experiment are made in panels a and b of Figure 5. For direct comparison between the Wigner threshold, free-particle treatment of ref 17, and the point dipole model, a scaling factor is used, but no other fitting of eq 10 to eq 9 is involved. The scaling factors change with temperature. We assume that similar observations are made in ref 17, but unfortunately, these were not reported. Nevertheless, comparison of the experimental trends in  $\sigma$  with the point dipole predictions does reveal the effect of temperature on the effective dipole moment. At 16 K, the best agreement between the point dipole model and experiment is clearly at  $D = 0.4$  a.u. (orange curve). At 295 K, however, the best agreement lies somewhere between 0.2 and 0.3 a.u. (green and purple). Increasing temperature and hence rotation are at least partly why a reduced dipole moment value gives rise to agreement with the experimental data for both  $\beta$  and  $\sigma$ .

In the asymptotic limit, the photoelectron wave function ( $\psi^{\text{el}}$ ) can be broken down into a superposition of pure orbital angular momentum components (partial waves). If  $\psi^{\text{el}}$  is purely s-wave in character,  $n$  in eq 10 equals 0.5 while  $\beta$  equals 0. If  $\psi^{\text{el}}$  is purely p-wave character,  $n = 1.5$  and  $\beta = 2$ . Within the free-electron approximation, we should expect s-wave character in  $\psi^{\text{el}}$  arising from p-character in the parent wave function while p-wave character in  $\psi^{\text{el}}$  arises from s-character in the parent wave function.

The free-electron treatment can be used to infer the effective character of the parent orbital. For  $\text{CN}^-$ , the almost instantaneous increase of  $\beta$  to near the limiting +2 indicates significant s-character in the parent orbital with a minor p-component. Increasing the dipole moment (of the neutral CN) will not alter the anion parent orbital but does lead to mixing of the angular momentum character of the continuum wave functions. This is seen in eq 6, where more than one  $A_{L_N, l}^\lambda$  for a given  $L_N^\lambda$  is non-zero. Of particular importance is the fact that the s-character of the parent allows increasing s-character in  $\psi^{\text{el}}$  as the dipole moment increases. This leads to a slower increase in  $\beta$  (with eKE) at higher dipole moments and more s-wave-like threshold behavior of the overall detachment cross section. More pertinently, in the context of eq 10, the lower the temperature, the greater the amount of s-character mixed into  $\psi^{\text{el}}$  and the lower the value of  $n$ .

The usual expectation for detachment from an anion  $\sigma$  orbital is a PAD with a positive  $\beta$ . This, rather low resolution, expectation is indeed borne out in the presented  $\text{CN}^-$  detachment data. On the contrary, the usual approach to quantitative prediction of the angular distribution (employing the free-electron approximation) clearly fails to recapture the finer details. Modeling the most important long-range interaction (electron–molecular dipole) with a point dipole description of the continuum clearly shows how the detachment process is affected by a polar molecule. The model introduced is, in principle, applicable to any molecular anion (through the use of the appropriate Dyson orbital). Although refinements (finite dipole treatment<sup>29,30</sup> and rotational transitions) will provide better accuracy, the model introduced here clearly shows that proper treatment of the PAD for anion detachment cannot ignore long-range effects.

## ■ ASSOCIATED CONTENT

### SI Supporting Information

The Supporting Information is available free of charge at <https://pubs.acs.org/doi/10.1021/acs.jpcllett.1c02882>.

Details of experimental techniques and data analysis (SI1) (PDF)

Derivation of the point dipole functions (SI2) (PDF)

Derivation of the photoelectron matrix elements using the point dipole functions (SI3) (PDF)

Derivation of the overall detachment cross section in the point dipole approximation (SI4) (PDF)

## ■ AUTHOR INFORMATION

### Corresponding Author

Richard Mabbs – Department of Chemistry, Washington University in St. Louis, St. Louis, Missouri 63132, United States; [orcid.org/0000-0002-1123-748X](https://orcid.org/0000-0002-1123-748X); Email: [mabbs@wustl.edu](mailto:mabbs@wustl.edu)

### Authors

C. Annie Hart – Department of Chemistry, Washington University in St. Louis, St. Louis, Missouri 63132, United States

Justin Lyle – Department of Chemistry, Washington University in St. Louis, St. Louis, Missouri 63132, United States; Present Address: J.L.: Intel Corp., Hillsboro, OR 97124

Joseph Spellberg – Department of Chemistry, Washington University in St. Louis, St. Louis, Missouri 63132, United States; Present Address: J.S.: Department of Chemistry,

The University of Chicago, 5735 S. Ellis Ave., Chicago, IL 60637.

Anna I. Krylov – Department of Chemistry, University of Southern California, Los Angeles, California 90089, United States; [orcid.org/0000-0001-6788-5016](https://orcid.org/0000-0001-6788-5016)

Complete contact information is available at: <https://pubs.acs.org/doi/10.1021/acs.jpcllett.1c02882>

## Notes

The authors declare the following competing financial interest(s): A.I.K. is the president and a part-owner of Q-Chem, Inc.

## ■ ACKNOWLEDGMENTS

This work was supported by the U.S. National Science Foundation (CHE-1856342 to A.I.K. and CHE-1566157 to R.M.).

## ■ REFERENCES

- (1) Wigner, E. P. On the behavior of cross sections near thresholds. *Phys. Rev.* **1948**, *73*, 1002–1009.
- (2) Surber, E.; Mabbs, R.; Sanov, A. Probing the molecular structure of small molecular anions by photoelectron imaging. *J. Phys. Chem. A* **2003**, *107*, 8215–8224.
- (3) Culberson, L. M.; Blackstone, C. C.; Sanov, A. Photoelectron Angular Distributions of Pyridinide: A Benchmark Application of the Mixed s-p Model to a Truly Polyatomic Anion. *J. Phys. Chem. A* **2013**, *117*, 11760–11765.
- (4) Grumbling, E. R.; Sanov, A. Photoelectron angular distributions in negative-ion photodetachment from mixed sp states. *J. Chem. Phys.* **2011**, *135*, 164302.
- (5) Khuseynov, D.; Blackstone, C. C.; Culberson, L. M.; Sanov, A. Photoelectron angular distributions for states of any mixed character: An experiment-friendly model for atomic, molecular, and cluster anions. *J. Chem. Phys.* **2014**, *141*, 124312.
- (6) Sanov, A.; Grumbling, E. R.; Goebbert, D. J.; Culberson, L. M. Photodetachment anisotropy for mixed s-p states: 8/3 and other fractions. *J. Chem. Phys.* **2013**, *138*, 054311.
- (7) Krylov, A. I. From orbitals to observables and back. *J. Chem. Phys.* **2020**, *153*, 080901.
- (8) Ortiz, J. V. Dyson-orbital concepts for description of electrons in molecules. *J. Chem. Phys.* **2020**, *153*, 070902.
- (9) Moitra, T.; Ponzi, A.; Koch, H.; Coriani, S.; Decleva, P. Accurate description of photoionization dynamical parameters. *J. Phys. Chem. Lett.* **2020**, *11*, 5330–5337.
- (10) Gozem, S.; Gunina, A. O.; Ichino, T.; Osborn, D. L.; Stanton, J. F.; Krylov, A. I. *J. Phys. Chem. Lett.* **2015**, *6*, 4532–4540.
- (11) Oana, C. M.; Krylov, A. I. Cross sections and photoelectron angular distributions in photodetachment from negative ions using equation of motion coupled cluster Dyson orbitals. *J. Chem. Phys.* **2009**, *131*, 124114.
- (12) Gozem, S.; Krylov, A. I. The ezSpectra suite: An easy-to-use toolkit for spectroscopy modeling. *Wiley Interdiscip. Rev.: Comput. Mol. Sci.* **2021**, 1546.
- (13) Bradforth, S. E.; Kim, E. H.; Arnold, D. W.; Neumark, D. M. Photoelectron spectroscopy of  $\text{CN}^-$ ,  $\text{NCO}^-$ , and  $\text{NCS}^-$ . *J. Chem. Phys.* **1993**, *98*, 800–810.
- (14) Huber, K. P.; Herzberg, G. *Molecular Spectra and Molecular Structure IV. Constants of Diatomic Molecules*; Van Nostrand Reinhold Co.: New York, 1979.
- (15) Harrison, S.; Tennyson, J. Electron collisions with the CN radical: bound states and resonances. *J. Phys. B: At., Mol. Opt. Phys.* **2012**, *45*, 035204.
- (16) Skomorowski, W.; Gulania, S.; Krylov, A. I. Bound and continuum-embedded states of cyanopolyyne anions. *Phys. Chem. Chem. Phys.* **2018**, *20*, 4805–4817.

(17) Simpson, M.; Notzold, M.; Schmidt-May, A.; Michaelsen, T.; Bastian, B.; Meyer, J.; Wild, R.; Gianturco, F. A.; Milovanovic, M.; Kokouline, V.; Wester, R. Threshold photodetachment spectroscopy of the astrochemical anion  $\text{CN}^-$ . *J. Chem. Phys.* **2020**, *153*, 184309.

(18) Krylov, A. I. Equation-of-motion coupled-cluster methods for open-shell and electronically excited species: the Hitchhiker's guide to Fock space. *Annu. Rev. Phys. Chem.* **2008**, *59*, 433–62.

(19) Shao, Y.; Gan, Z.; Epifanovsky, E.; Gilbert, A. T. B.; Wormit, M.; Kussmann, J.; Lange, A. W.; Behn, A.; Deng, J.; Feng, X.; et al. Advances in molecular quantum chemistry contained in the Q-Chem 4 program package. *Mol. Phys.* **2015**, *113*, 184–215.

(20) Liu, Y.; Ning, C. Calculation of photodetachment cross sections and photoelectron angular distributions of negative ions using density functional theory. *J. Chem. Phys.* **2015**, *143*, 144310.

(21) Cohen-Tannoudji, C.; Fdiu, B.; Laloe, F. *Quantum Mechanics*; John Wiley & Sons: New York, 1977; Vol. II.

(22) Mittleman, M. H.; von Holdt, R. E. Theory of low-energy electron scattering by polar molecules. *Phys. Rev.* **1965**, *140*, A726–A729.

(23) Siegel, J.; Dehmer, J. L.; Dill, D. Hybrid calculation of electron polar-molecule scattering: Integrated and momentum-transfer cross sections for LiF. *Phys. Rev. A: At, Mol, Opt. Phys.* **1981**, *23*, 632–640.

(24) Fermi, E.; Teller, E. The capture of negative mesotrons in matter. *Phys. Rev.* **1947**, *72*, 399–408.

(25) Crawford, O. H. Negative ions of polar molecules. *Mol. Phys.* **1971**, *20*, 585–591.

(26) Crawford, O. H.; Garrett, W. R. Electron affinities of polar molecules. *J. Chem. Phys.* **1977**, *66*, 4968–4970.

(27) Simons, J. Molecular anions. *J. Phys. Chem. A* **2008**, *112*, 6401–6511.

(28) Jordan, K. D.; Wang, F. Theory of dipole-bound anions. *Annu. Rev. Phys. Chem.* **2003**, *54*, 367–396.

(29) Patil, S. H. An electron in a finite dipole potential. *J. Chem. Phys.* **2004**, *120*, 6399–6407.

(30) Schumayer, D.; van Zyl, B. P.; Bhaduri, R. K.; Hutchinson, D. A. W. Geometric scaling in the spectrum of an electron captured by a stationary finite dipole. *EPL* **2010**, *89*, 13001.